Author/s:
Wasko, C;Parinussa, RM;Sharma, A

Title:
A quasi-global assessment of changes in remotely sensed rainfall extremes with temperature

Date:
2016-12-28

Citation:
Wasko, C., Parinussa, R. M. & Sharma, A. (2016). A quasi-global assessment of changes in remotely sensed rainfall extremes with temperature. Geophysical Research Letters, 43 (24), pp.12-668. https://doi.org/10.1002/2016GL071354.

Persistent Link:
https://hdl.handle.net/11343/292266

A quasi-global assessment of changes in remotely sensed rainfall extremes with temperature

C. Wasko[1], R.M. Parinussa[1, 2], and A. Sharma[1]

[1]School of Civil and Environmental Engineering, University of New South Wales, Australia.

[2]Van der Sat B.V., Space Technology Business Park, Noordwijk, The Netherlands.

Corresponding author: Conrad Wasko (conrad.wasko@unsw.edu.au)

Key Points:

- The dependence of rainfall to temperature in remotely sensed products is compared to ground observations
- Spatial inhomogeneity in the dependence of rainfall on temperature is preserved in remotely sensed products
- Sensitivities to duration and percentile are explored

This is the author manuscript accepted for publication and has undergone full peer review but has not been through the copyediting, typesetting, pagination and proofreading process, which may lead to differences between this version and the Version of Record. Please cite this article as doi: 10.1002/2016GL071354

Abstract

The dependence between extreme rainfall and temperature is used to understand climatic relationships, constrain model predictions and evaluate future changes to rainfall. Understanding this dependence, however, is limited by the fact that many areas worldwide lack gauged data, particularly at short time scales. The advent of remote sensing allows a new insight into this dependence quasi-globally. Here, we address whether remotely sensed daily rainfall and temperature can be used in ungauged areas to understand extreme rainfall scaling with temperature. Using the multi-sensor Tropical Rainfall Measuring Mission 3B42 (v7) rainfall product and remotely sensed air temperature we examine the spatial homogeneity in remotely sensed rainfall scaling with temperature and demonstrate that it replicates the spatial variation in the scaling observed in ground data. Finally, changes to duration and percentile are examined showing that the scaling response is climatologically sensitive.

1 Introduction

Rainfall and air temperature correlations help build an understanding of climate interactions with higher temperatures often related to greater variability in rainfall [*Trenberth and Shea*, 2005; *King et al.*, 2014]. Rainfall and temperature relationships aid model evaluation [*Allen and Ingram*, 2002; *O'Gorman*, 2012] and are used to understand the mechanics of extreme rainfall generation [*Lenderink and van Meijgaard*, 2008; *Berg et al.*, 2013; *Wasko and Sharma*, 2015; *Wasko et al.*, 2016]. It has been shown that historical trends in rainfall correlate well with

historical trends in temperature [*Wentz et al.*, 2007; *Lenderink et al.*, 2011; *Westra and Sisson*, 2011; *Benestad*, 2013; *Lenderink and Attema*, 2015].

As intense rainfall is the primary driver of catastrophic flooding, particularly in urban areas, there is significant interest in looking at the dependence of extreme rainfall with air temperature termed scaling [*Seneviratne et al.*, 2012; *Westra et al.*, 2014]. This is because extreme rainfall intensity is linked to the atmospheric water vapor content which in turn is linked to temperature thermodynamically through the Clausius-Clapeyron relationship [*Allen and Ingram*, 2002; *O'Gorman and Schneider*, 2009]. Departures from the Clausius-Clapeyron relationship are common and for example attributed to dynamic factors such as storm intensification and spatial shifts in large-scale circulation such as storm tracks [*Trenberth et al.*, 2003]. Hence scaling relationships are frequently used to postulate how rainfall extremes may change if temperatures increase in a future climate [*Berg et al.*, 2013; *Lenderink and Attema*, 2015; *Molnar et al.*, 2015; *Wasko et al.*, 2015; *Busuioc et al.*, 2016].

Rainfall-temperature scaling varies significantly with local climate [*Mishra et al.*, 2012]. On a global scale, scaling is generally positive indicating larger rainfall intensities at higher temperatures, with negative scaling observed in tropical areas, indicating smaller rainfall intensities at higher temperatures [*Utsumi et al.*, 2011; *Maeda et al.*, 2012]. Results show, in general, increasing scaling as the percentile considered becomes more extreme [*Hardwick Jones et al.*, 2010; *Busuioc et al.*, 2016], and decreasing scaling with increasing duration [*Hardwick Jones et al.*, 2010; *Panthou et al.*, 2014; *Wasko et al.*, 2015], although these results are climate

specific, with decreases as the percentile increases shown locally [*Shaw et al.*, 2011; *Maeda et al.*, 2012]. Negative scaling of rainfall at higher temperatures has been shown to correlate with reductions in humidity [*Hardwick Jones et al.*, 2010], particularly at longer durations [*Wasko et al.*, 2015], as well as being related to dynamical effects due to orography [*Drobinski et al.*, 2016]. In dry regions, however, the negative scaling can be due to the fact that when less rainfall occurs there is more sunlight, resulting in less soil moisture, and a higher surface air temperature [*Trenberth and Shea*, 2005]. Storm type [*Berg et al.*, 2013; *Molnar et al.*, 2015], season [*Berg et al.*, 2009; *Wasko and Sharma*, 2014], and large-scale circulations [*Blenkinsop et al.*, 2015] also modulate the scaling relationship. This lack of generality is not surprising given the number of factors that interact with rainfall [*Tan and Shao*, 2016] and the complex nature of feedbacks between precipitation, evaporation, soil moisture and temperature which prevent universal cause and effect relationships to be described [*Trenberth and Shea*, 2005].

The majority of studies that evaluate the scaling of extreme rainfall with temperature use gauged point observations, or alternatively, aggregate point observations losing spatial variability [*Utsumi et al.*, 2011; *Westra et al.*, 2014; *Blenkinsop et al.*, 2015]. With the advent of rainfall remote sensing it is now possible to extend scaling relationships and their related applications to ungauged areas. However, as far as the authors are aware, the applications of remotely sensed products to extreme rainfall scaling is limited, possibly due to the large data sets which are required when extreme percentiles are investigated. Here, we focus on the multi-sensor Tropical Rainfall Measuring Mission (TRMM) 3B42 (v7) rainfall product based on observations of

visible and infrared scanners as well as observations of multiple passive microwave sensors [*Kummerow et al.*, 1998; *Huffman et al.*, 2007]. The TRMM satellite plays a key role within this 3B42 product which was launched in 1997 and provides a 3 hourly continuous and global rainfall data set. This 3B42 dataset is expected to be replaced by the Integrated Multi-satellitE Retrievals from the Global Precipitation Measurement Mission (IMERG) [*Hou et al.*, 2014]. The ability of 3B42 to measure rainfall at resolutions and in areas that previously could not be measured [*Nicholson et al.*, 2003; *Bookhagen and Burbank*, 2006] has allowed the creation of unprecedented data sets for forcing global land models [*Sheffield et al.*, 2006], and the calculation of design rainfall relationships in data sparse regions [*Awadallah and Awadallah*, 2013]. The use of 3B42 has been thoroughly tested in hydrology with rainfall amounts [*Huffman et al.*, 2007], rainfall event timing [*Libertino et al.*, 2016], and suitability for hydrological modelling [*Collischonn et al.*, 2008; *Su et al.*, 2008; *Li et al.*, 2013; *Zulkafli et al.*, 2014] all evaluated. TRMM 3B42 correlates well with gauge products, although appearing to underestimate extreme rainfall [*Romilly and Gebremichael*, 2011; *Ward et al.*, 2011; *Prasetia et al.*, 2013; *Lo Conti et al.*, 2014] particularly when deep convection is present [*Rasmussen et al.*, 2013]. In general it is found that TRMM 3B42 performs better at greater temporal [*Lo Conti et al.*, 2014; *Ochoa et al.*, 2014] and spatial aggregations [*Fleming et al.*, 2011; *Liu and Allan*, 2012], and over oceans [*Tian and Peters-Lidard*, 2010].

Regional and global studies of precipitation sensitives with temperature have been performed [*Liu and Allan*, 2012; *O'Gorman*, 2012] with sensitivities of up to 23%K^{-1} observed [*Liu et al.*,

2009]. The TRMM 3B42 rainfall product has also been used to relate annual rainfall [*Lau and Wu*, 2011] and tropical cyclone activity [*Lin et al.*, 2015] to sea surface temperatures. However, as far as the authors are aware, a fine resolution pixel by pixel study of the rainfall-temperature relationship in remotely sensed data remains to be performed. In this manuscript we compare the scaling of TRMM 3B42 rainfall with ground observations to answer the question: can remote sensing complement ground observations for prediction of extreme rainfall scaling by providing a quasi-global map of rainfall-temperature scaling? Following a comparison focusing on the spatial distribution of scaling we assess the variability in scaling with duration and percentile on a quasi-global scale.

2 Data and methods

Remotely sensed rainfall is sourced from the Tropical Rainfall Monitoring Mission (TRMM) 3B42 (v7) product. The 3B42 algorithm [*Huffman et al.*, 2007] converts remotely sensed observations to rainfall rates and consists of two separate steps. First, the TRMM Visible and Infrared Scanner (VIRS) and Microwave Imager (MI) observations are combined to produce calibration parameters. The next step uses these parameters to adjust a merged Infrared datasets from various geostationary satellite platforms into rainfall rates. Finally, the adjusted merged Infrared products at a 0.25° spatial resolution are rescaled to match monthly ground observations and 3 hourly time-steps centered on the synoptic UTC time are aggregated into daily representations. These observations are accumulated to daily for the time period of 1998-2014 inclusive. Where three-hourly observations are considered in this manuscript daily maximum

three hourly observations are used. Unlike the polar orbiting Aqua satellite, TRMM is in a (near) equatorial orbit. TRMM satellite orbit is in a constant plane relative to the sun covering the latitudes between 50° north and 50° south which was subsequently the region over which this study was performed.

The other remotely sensed dataset used in this study was obtained through observations of the Atmospheric Infrared Sounder (AIRS) spectrometer mounted onboard the polar orbiting Aqua satellite. Despite known sampling issues under clouds as infrared only samples clear sky conditions (not necessarily consistent with rainfall events) [e.g *Yue et al.*, 2013] the AIRS temperature product was chosen for its long term consistency compared to other remotely sensed products, especially at the quasi-global scale. AIRS observations were combined with observations from the Advanced Microwave Sounding Unit (AMSU) and the Humidity Sounder for Brazil (HSB) resulting in a range of remotely sensed observations related to atmospheric conditions. These remotely sensed observations were related to daily surface air temperature at a global 1°×1° degree spatial resolution [*AIRS Science Team/Joao Texeira*, 2013] and were obtained through the NASA Goddard Earth Science Data and Information Services Centre (GES DISC; Version 6). Each daily datafile covers a 24 hour period including an ascending and a descending satellite path with an equatorial crossing of 01:30 PM (day-time) and 01:30 AM (night-time) respectively. In this study, the daily night-time surface air temperatures were used. Night-time temperatures are preferred as they are more spatially homogenous due to the absence of cooling induced by transpiration during the day.

Due to differences in availability and data characteristics (temporal and spatial resolution) of each dataset, compromises had to be made. The spatial resolution of the AIRS surface air temperature is lowest but was resampled to match the TRMM 3B42 rainfall product. Daily and three hourly rainfall observations were matched to the coincident daily temperature observation at the grid cell of interest and only days where the rainfall was non-zero were used. Ground observations of rainfall were obtained from the Global Historical Climatology Network (GHCN) [*Menne et al.*, 2012, 2015]. All available data from ground stations with more than ten years of data was used resulting in a total of 39632 stations. All non-zero rainfall days were matched to their coincident temperature. The temperature used was from the nearest 1°×1° grid square from the Berkeley Earth gridded average daily temperature data set [*Rohde et al.*, 2013a, 2013b; *Berkeley Earth*, 2015]. Although night-time temperatures may not correspond to the daily average temperature it has been shown scaling relationships are largely insensitive to diurnal fluctuations [*Hardwick Jones et al.*, 2010; *Wasko and Sharma*, 2014]. Verification (not shown) using temperature from the nearest 1°×1° grid square rather than at site gauge temperature was performed using point observations of temperature measured by Australia's Bureau of Meteorology. The scaling were found to be similar regardless of the temperature product used.

The rainfall-temperature scaling was determined at each grid cell or gauge site using quantile regression [*Koenker and Bassett*, 1978; *Koenker*, 2013; *Wasko and Sharma*, 2014] where the rainfall was log-transformed [*Lenderink and van Meijgaard*, 2008; *Hardwick Jones et al.*, 2010; *Utsumi et al.*, 2011]. The temperature range used was either below 24°C or above 24°C with

scaling determined at each site for the range which contained the majority of the data. This is because it has been shown that the rainfall-temperature relationship is generally positive below 24°C and negative above this temperature [*Lenderink et al.*, 2011; *Panthou et al.*, 2014; *Westra et al.*, 2014]. Though reasons for this reversal are debated [*Berg et al.*, 2009], the decrease in the scaling above 24°C has been correlated with a reduction in relative humidity [*Hardwick Jones et al.*, 2010], and absolute humidity [*Wasko et al.*, 2015], suggesting that moisture availability does not endlessly increase with temperature, at least for interannual variability [*Westra et al.*, 2014; *Drobinski et al.*, 2016].

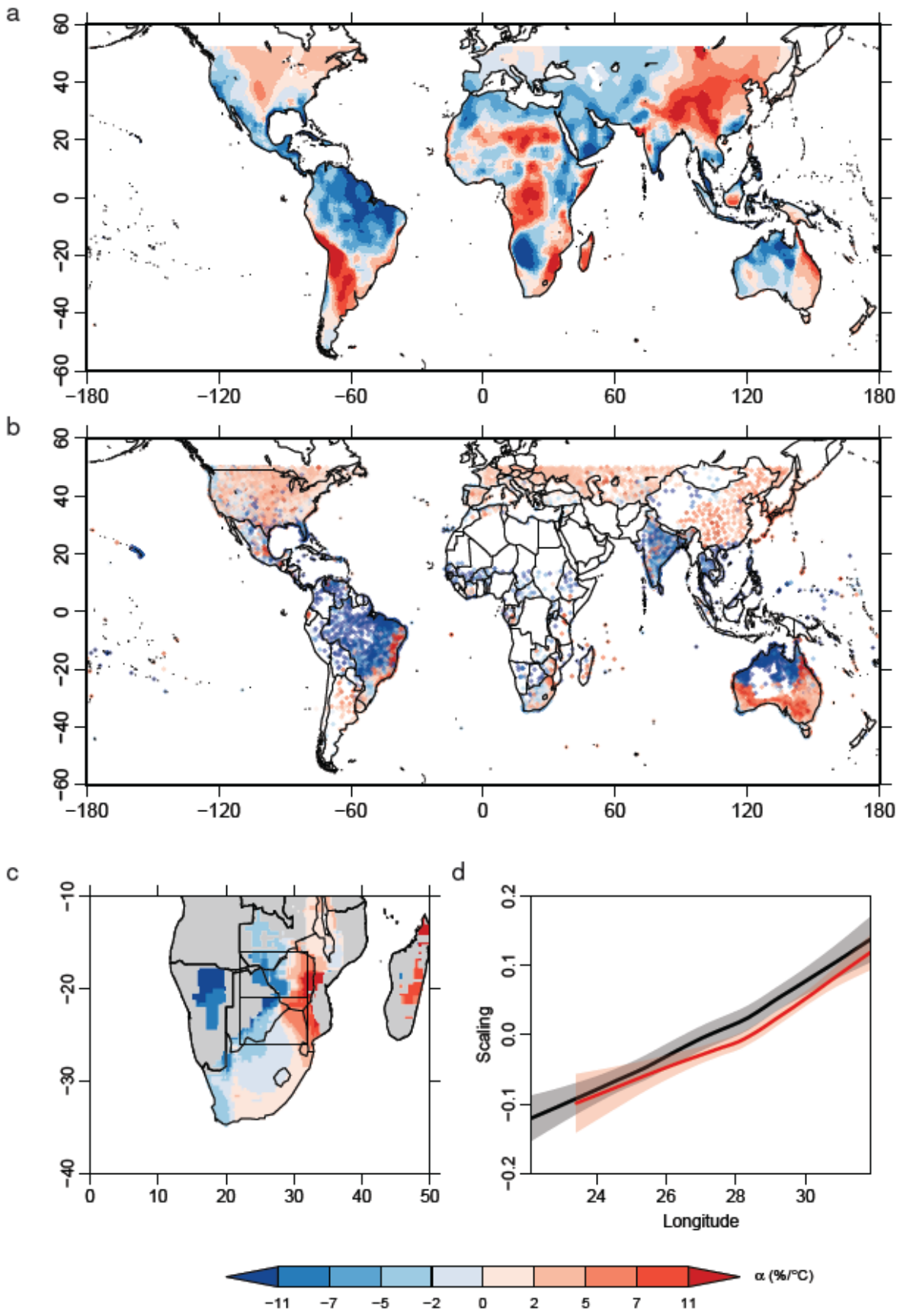

Figure 1. Precipitation-temperature scaling for the 90th percentile. (a) Remotely sensed 3B42 data averaged using a 4° × 4° running median (b) Ground data (c) 4° × 4° degree median smooth of ground data over southern Africa (d) 3B42 scaling (black) and ground observations (red) plotted against longitude for box shown in (c). Fitted lines are the result of local linear regression with 99% confidence intervals shaded.

3 Comparison of TRMM scaling with ground observations

The scaling for the 90th percentile using all non-zero 3B42 rainfall days is presented in Figure 1a. A running median on a moving 4° × 4° grid has been used to smooth out variability. The raw results alongside the smoothed results are presented in Figure S1. There is large spatial inhomogeneity with negative scaling not constrained to the equatorial regions. For example, Australia's west coast exhibits negative rainfall scaling, where average ground temperatures are higher, and exhibits positive scaling on the east coast where average ground temperatures are lower. Large areas of the Middle East, Europe and Central America show negative scaling also. There tends to be positive scaling in regions of greater elevation, generally associated with lower average ground temperatures, such as the Himalayas. North America has a negative scaling on the west coast and a positive scaling in the center of its land mass.

Here we are interested in whether these patterns are similar to those in the ground observations. Figure 1b presents the 90th percentile scaling for all the gauge data sites using all available data. Figure S2 presents a replicate of Figure 1b using only data post 1998 to better match the date range of the 3B42 rainfall. For the durations considered here, the correspondence between Figure 1b and Figure S2 suggests the different sampling duration does not bias the scaling in the ground

observations. We proceed with Figure 1b which uses the entire time series of each gauge and provides a greater number of comparison sites, despite less consistent sampling. Despite the large amount of sub-grid variability the scaling in the southern hemisphere matches very well. It appears for the continents of South America, Africa and Australia the change in scaling on the east coast from negative to positive (west to east) has been captured. In particular, the narrow region of positive scaling along the east coast of South America and Australia present in the ground observations is replicated as is the higher scaling in the central U.S., Eastern Asia and in particular around the Korean Peninsula. There appears to be reasonable agreement in North America with lower scaling along the west coast and the local negative scaling around the Gulf of Mexico. However, in Europe the direction of the scaling is not replicated with positive ground observation scaling and negative remotely sensed scaling.

The ability of 3B42 scaling to capture the ground scaling spatial inhomogeneity is presented in Figure 1c and Figure 1d. Regions of central and southern Africa are well known as data sparse regions. In this area the scaling changes direction from negative to positive in a west to east direction. Using the same 0.25° × 0.25° 3B42 data grid Figure 1c presents a running 4° × 4° median smooth on the ground observation scaling presented in Figure 1b. The median is determined for a grid cell if there are five or more gauge sites within the cell. There is mutual agreement between this spatial variation and the one presented for the 3B42 data in Figure 1a. This is confirmed by plotting the scaling against longitude. Figure 1d presents a fitted local linear regression for the 3B42 data (black) and the ground observations (red) for the box presented in

Figure 1c. The shading represents the computed 99th percentile confidence limits. For both the remotely sensed and ground observations, the scaling transitions from positive to negative, east to west. Although the absolute magnitude does not match, the results are similar, and the spatial variation is captured by the 3B42 data. Similar results are presented for South America (Brazil) and India in Figure S3.

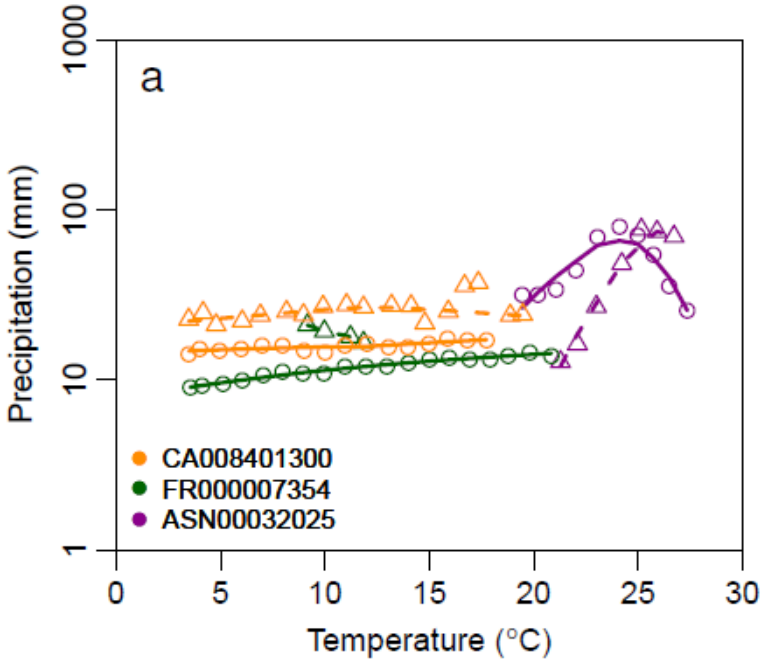

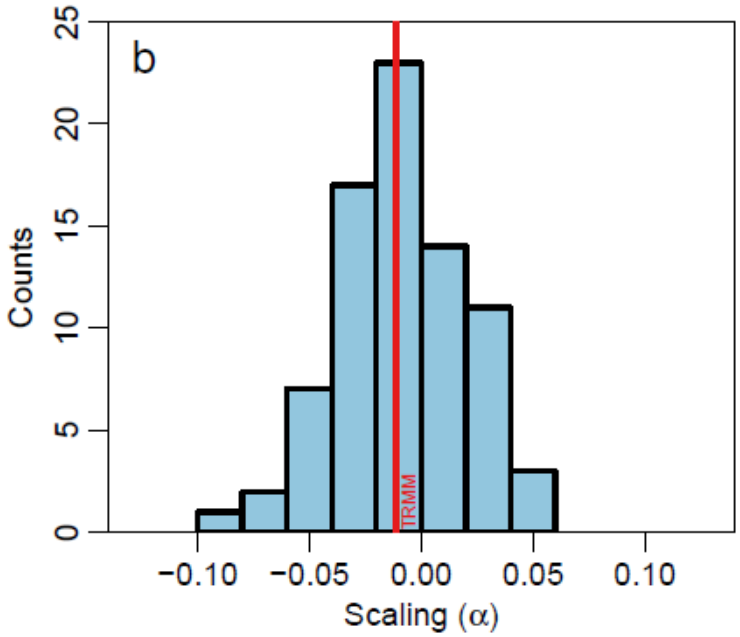

Figure 2. (a) Comparison of 90th percentile scaling of 3B42 and ground observations for three locations. Triangles are 3B42 data, circles are ground observations. Fitted lines are a local linear regression. (b) Histogram of scaling for a single 0.25° × 0.25° grid cell centered on 151.125°, -33.825°. The red line is the scaling for the 3B42 data observed at that grid cell.

The scaling for three sites whose details are summarized in Table S1 is presented in Figure 2a. Broadly speaking the sites are located in far east of southern Canada (yellow), central France (green) and north eastern Australia (purple). The 90th percentile is determined at each degree Celsius using a two degree temperature window for both the 3B42 (triangles) and ground (circles) observations. The fitted lines are a local linear regression (LOESS) and the 3B42 data is from the grid cell containing the ground observation site. The Canadian site is an example of where the scaling is well replicated by the remote sensed data. Although there is more variability in the 3B42 data (a result of less data being available), the temperature ranges are similar and the trend with increasing temperature is similar to that in the ground observations. We can be confident that the scaling determined from the remotely sensed data is representative of the scaling determined from ground observations.

However, in central regions in Europe the scaling is not well captured. The site in France presented in green is one such example. The remote sensing data predicts negative scaling while the ground data scales positively. The remotely sensed data does not span a large enough temperature range to make conclusions on the scaling and there are an insufficient number of observations. This site illustrates the difficulty in capturing the scaling exhibited by ground

observations with limited remotely sensed data. The final station, located in Australia, presents an example of the scaling reversal. Both the 3B42 rainfall and ground observations show a reversal in scaling around 24°C. The peak point temperature is well represented in the 3B42 data, however, the amount of data post reversal is simply not enough to determine the scaling past this point. In this situation the ground data suggests a reversal and intuitively we expect similar behavior in the 3B42 data, but without this prior knowledge the reversal would be difficult to visually identify.

Rainfall variability also presents difficulties in the comparison of 3B42 scaling with ground observations. Figure 2b presents the scaling for a single 0.25° × 0.25° TRMM cell (centered on 151.125°, -33.825°) for Sydney, Australia. This location is chosen as it has the single largest number of ground observations within it - a total of 78 gauge stations. The scaling for all the stations within the grid cell is presented as a histogram and the single 3B42 scaling observation is presented a red vertical line. It is not possible to capture the large variability in the scaling measured by the ground observations as the 3B42 observations are over a larger spatial scale. The 3B42 scaling clearly lies within the range of expected values, but, if we consider the possibility that only one site in this sample was available for evaluation, a close match between the 3B42 scaling and ground observations would be unlikely.

4 Sensitivity of TRMM scaling to duration and percentile

We present a quasi-global assessment of the change in scaling with decreasing duration. Using 3B42 data, the difference between the 3 hour and 24 hour scaling for the 90th percentile is presented in Figure 3. In the tropics, a region generally experiencing a larger proportion of convective events [*Zipser et al.*, 2006], there is an increase in the scaling for the 3 hour duration when compared to the 24 hour duration, with the magnitude of this increase greater closer to the equator. In the subtropics and temperate regions there is a small decrease in the scaling. However, the magnitude of this decrease is very small and rarely greater than 0.02 (or 2%), in contrast to the increases in the tropical regions where the magnitude of the increase is much higher.

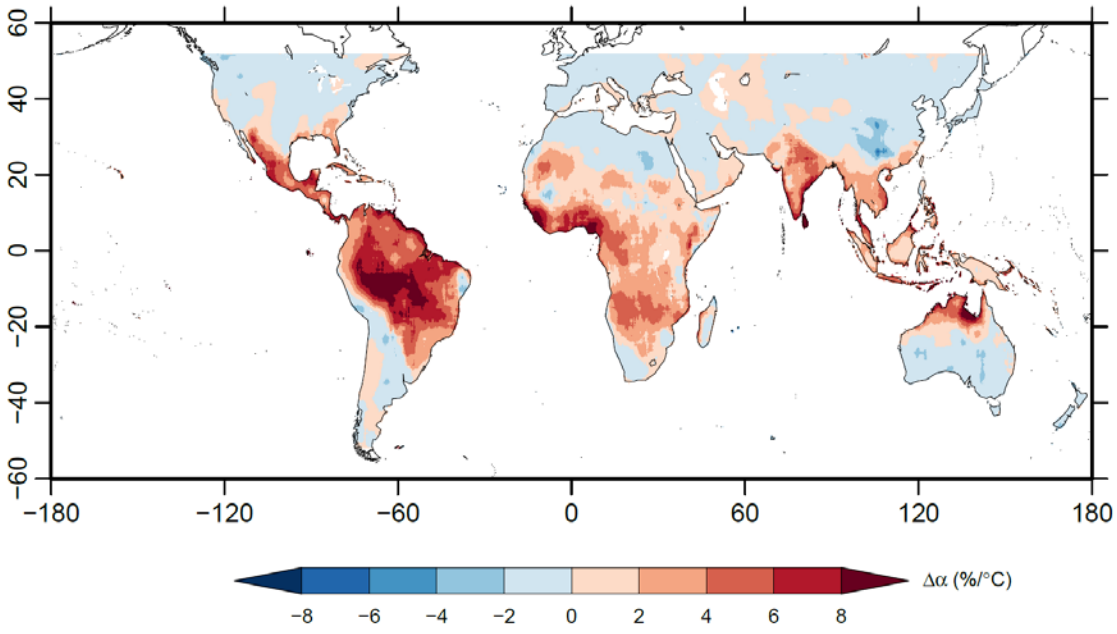

Figure 3. Three hour scaling minus 24 hour scaling for the 90th percentile. Results have been smoothed using a 4° × 4° running median.

To assess more extreme percentiles there is a need to accumulate the data. Similar to previous studies in this field, data is accumulated from a spatial region, in this case from a 0.25° × 0.25° grid to a 1° × 1° grid, effectively increasing our data at each scaling evaluation grid cell 16 fold. The validation of the aggregation is presented in Figure S1. The scaling determined from the 1° × 1° grid, with a 4° × 4° running median smoother is presented in Figure S1c. The original 0.25° × 0.25° grid scaling (Figure S1b) and that obtained from the 1° × 1° degree grid (Figure S1c) are similar, despite being obtained from different resolutions. For example, the transition of scaling from negative to positive in an easterly direction on the east coasts of South America, Africa and Australia is captured. Despite a loss in resolution across Asia due to the aggregation, there is now a slightly greater scaling in Europe which better matches the ground observations. This confirms that a lack of data, in particular, a lack of temperature range in the remotely sensed data, is at least partially responsible for not capturing the rainfall scaling of ground observations. Most importantly, the close agreement between the two different grid sizes confirms that the scaling determined from the aggregated data is representative and can be used for calculating more extreme percentiles.

The differences for the 99^{th} and 99.9^{th} percentile scaling compared to the 90^{th} percentile are presented in Figure 4. The differences appear local climate specific. For example, in Australia, increases are seen throughout the continent with the exception of the eastern sea board. This

spatial variation appears similar to the pattern of scaling presented in Figure 1a. Those areas with positive scaling show a decrease with increasing percentile, while those areas that had a negative scaling show an increase. This pattern intensifies as the percentile considered becomes more extreme (Figure 4b). The results are consistent with *Maeda et al.*, [2012] who found reduced negative scaling when considering more extreme percentiles. As event type can have significant effects on the scaling obtained [*Molnar et al.*, 2015], it has been suggested this may be the result of more consistent sampling of a particular type of meteorological event or weather system at the most extreme percentiles [*Shaw et al.*, 2011],

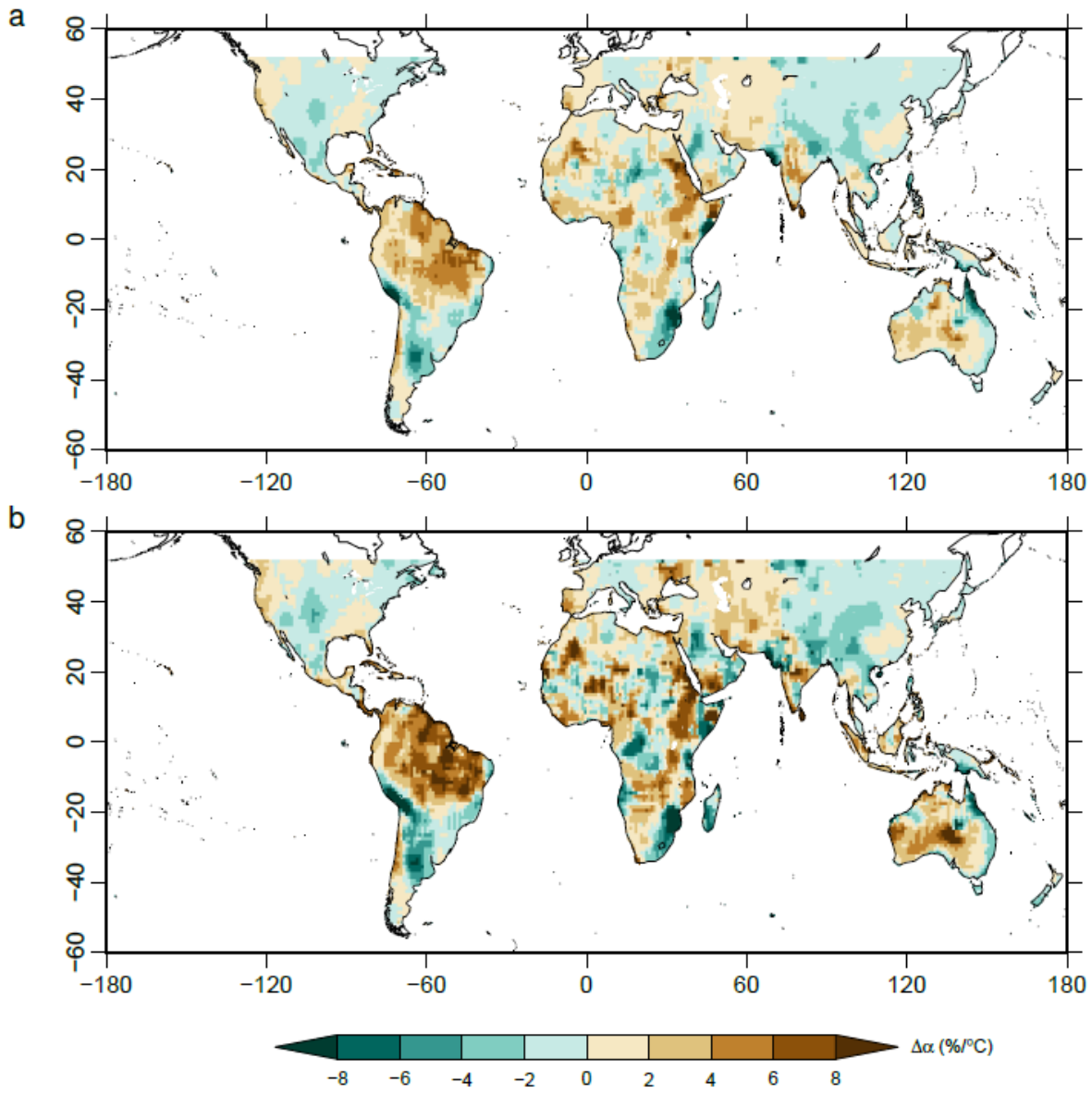

Figure 4. Difference from 90th percentile scaling. (a) 99th percentile (b) 99.9th percentile. Results have been smoothed using a 4° × 4° running median.

5 Discussion and conclusions

The dependence between rainfall and temperature is exploited for many applications from constraining models to evaluating rainfall changes for a future climate. Here we present a quasi-global assessment of extreme rainfall percentile scaling with temperature. Several regions show that the large spatial inhomogeneity in the scaling relationship in ground observations is remarkably well captured by the relatively short record of TRMM 3B42 rainfall measurements. As ground observations are often unavailable, this is encouraging, and suggests that remotely sensed rainfall-temperature relationships may be used where ground observations are unavailable. Despite these promising results there are several regions where discrepancies remain. For example, the remotely sensed data underestimates the scaling throughout regions of Europe. Improvements were shown when the remotely sensed data was accumulated to a larger spatial scale, possibly due to the larger sample size resulting in a better capture of temperature variability. However, due to differences in the spatial scale of the ground observations and remotely sensed data, internal satellite pixel variability will inevitably result in mismatches when single sites are considered. As the spatial variation of the ground observation scaling, even at sub-grid scale, is large, ground observations will likely continue to be used preferentially. This is particularly true where multiple gauge observations can be used to obtain robust scaling estimates [*Roth et al.*, 2015].

The sensitivity of the rainfall scaling to duration was presented by comparing the maximum three hourly TRMM rainfall scaling to the accumulated daily rainfall scaling. The scaling increased in tropical areas but decreased in regions outside the tropics. However, the magnitude of the

decrease was much less than the increase observed in the tropical areas. To assess more extreme percentiles aggregation was performed. Validation against the original 3B42 rainfall resolution showed that aggregation did not deteriorate the quality of the scaling prediction, and even improved it in some areas due to greater data availability. It was found, in general, where strong positive scaling exists, a decrease in the scaling with increasing extreme percentile is observed, but an increase in the scaling is observed in regions of negative scaling.

Given the strong dependence between rainfall and temperature and the ability to estimate the scaling relationship at extreme percentiles using remotely sensed TRMM 3B42 rainfall, rainfall-temperature relationships can be developed in data spare regions. These relationships can then be used to investigate climate interactions and form the basis for understanding how rainfall responds to changes in temperature in regions that previously could not be investigated.

Acknowledgments and Data

The authors acknowledge financial support of the Australian Research Council. TRMM 3B42 rainfall is available at https://pmm.nasa.gov/TRMM and AIRS temperature data at http://dx.doi.org/10.5067/QUA/AIRS/DATA207. The GHCN data set is available in *Menne et al.*[2015] and temperature data in *Berkeley Earth* [2015]. The authors would like to thank the anonymous reviewers whose feedback greatly improved the quality of this manuscript.

Figure Captions

Figure 1. Precipitation-temperature scaling for the 90th percentile. (a) Remotely sensed 3B42 data averaged using a 4° × 4° running median (b) Ground data (c) 4° × 4° degree median smooth of ground data over southern Africa (d) 3B42 scaling (black) and ground observations (red) plotted against longitude for box shown in (c). Fitted lines are the result of local linear regression with 99% confidence intervals shaded.

Figure 2. (a) Comparison of 90th percentile scaling of 3B42 and ground observations for three locations. Triangles are 3B42 data, circles are ground observations. Fitted lines are a local linear regression. (b) Histogram of scaling for a single 0.25° × 0.25° grid cell centered on 151.125°, -33.825°. The red line is the scaling for the 3B42 data observed at that grid cell.

Figure 3. Three hour scaling minus 24 hour scaling for the 90th percentile. Results have been smoothed using a 4° × 4° running median.

Figure 4. Difference from 90th percentile scaling. (a) 99th percentile (b) 99.9th percentile. Results have been smoothed using a 4° × 4° running median.

References

AIRS Science Team/Joao Texeira (2013), *AIRS/Aqua L3 Daily Standard Physical Retrieval (AIRS-only) 1 degree x 1 degree V006*, NASA Goddard Earth Science Data and Information Services Center (GES DISC), Greenbelt, MD, USA.

Allen, M. R., and W. J. Ingram (2002), Constraints on future changes in climate and the hydrologic cycle, *Nature*, *419*(6903), 224–232, doi:10.1038/nature01092.

Awadallah, A. G., and N. A. Awadallah (2013), A Novel Approach for the Joint Use of Rainfall Monthly and Daily Ground Station Data with TRMM Data to Generate IDF Estimates in a Poorly Gauged Arid Region, *Open J. Mod. Hydrol.*, *2013*(January), 1–7.

Benestad, R. E. (2013), Association between trends in daily rainfall percentiles and the global mean temperature, *J. Geophys. Res. Atmos.*, *118*(19), 10,802-10,810, doi:10.1002/jgrd.50814.

Berg, P., J. O. Haerter, P. Thejll, C. Piani, S. Hagemann, and J. H. Christensen (2009), Seasonal characteristics of the relationship between daily precipitation intensity and surface temperature, *J. Geophys. Res.*, *114*, D18102, doi:10.1029/2009JD012008.

Berg, P., C. Moseley, and J. O. Haerter (2013), Strong increase in convective precipitation in response to higher temperatures, *Nat. Geosci.*, *6*(3), 181–185, doi:10.1038/ngeo1731.

Berkeley Earth (2015), *Berkeley Earth Project*, [available at http://berkeleyearth.org/data/].

Blenkinsop, S., S. C. Chan, E. J. Kendon, N. M. Roberts, and H. J. Fowler (2015), Temperature influences on intense UK hourly precipitation and dependency on large-scale circulation, *Environ. Res. Lett.*, *10*(5), 54021, doi:10.1088/1748-9326/10/5/054021.

Bookhagen, B., and D. W. Burbank (2006), Topography, relief, and TRMM-derived rainfall variations along the Himalaya, *Geophys. Res. Lett.*, *33*(8), 1–5,

doi:10.1029/2006GL026037.

Busuioc, A., M. V. Birsan, D. Carbunaru, M. Baciu, and A. Orzan (2016), Changes in the large-scale thermodynamic instability and connection with rain shower frequency over Romania: Verification of the Clausius-Clapeyron scaling, *Int. J. Climatol.*, *2034*(September 2015), 2015–2034, doi:10.1002/joc.4477.

Collischonn, B., W. Collischonn, and C. E. M. Tucci (2008), Daily hydrological modeling in the Amazon basin using TRMM rainfall estimates, *J. Hydrol.*, *360*(1–4), 207–216, doi:10.1016/j.jhydrol.2008.07.032.

Lo Conti, F., K.-L. Hsu, L. V. Noto, and S. Sorooshian (2014), Evaluation and comparison of satellite precipitation estimates with reference to a local area in the Mediterranean Sea, *Atmos. Res.*, *138*, 189–204, doi:10.1016/j.atmosres.2013.11.011.

Drobinski, P., B. Alonzo, S. Bastin, N. Da Silva, and C. Muller (2016), Scaling of precipitation extremes with temperature in the French Mediterranean region: What explains the hook shape?, *J. Geophys. Res. Atmos.*, *121*(7), 3100–3119, doi:10.1002/2015JD023497.

Fleming, K., J. L. Awange, M. Kuhn, and W. E. Featherstone (2011), Evaluating the TRMM 3B43 monthly precipitation product using gridded rain-gauge data over Australia, *Aust. Meteorol. Oceanogr. J.*, *49*, 171–184.

Hardwick Jones, R., S. Westra, and A. Sharma (2010), Observed relationships between extreme sub-daily precipitation, surface temperature, and relative humidity, *Geophys. Res. Lett.*,

37(22), L22805, doi:10.1029/2010GL045081.

Hou, A. Y., R. K. Kakar, S. Neeck, A. A. Azarbarzin, C. D. Kummerow, M. Kojima, R. Oki, K. Nakamura, and T. Iguchi (2014), The Global Precipitation Measurement Mission, *Bull. Am. Meteorol. Soc.*, *95*(5), 701–722, doi:10.1175/BAMS-D-13-00164.1.

Huffman, G. J., D. T. Bolvin, E. J. Nelkin, D. B. Wolff, R. F. Adler, G. Gu, Y. Hong, K. P. Bowman, and E. F. Stocker (2007), The TRMM Multisatellite Precipitation Analysis (TMPA): Quasi-Global, Multiyear, Combined-Sensor Precipitation Estimates at Fine Scales, *J. Hydrometeorol.*, *8*(1), 38–55, doi:10.1175/JHM560.1.

King, A. D., N. P. Klingaman, L. V. Alexander, M. G. Donat, N. C. Jourdain, and P. Maher (2014), Extreme Rainfall Variability in Australia: Patterns, Drivers, and Predictability, *J. Clim.*, *27*(15), 6035–6050, doi:10.1175/JCLI-D-13-00715.1.

Koenker, R. (2013), *quantreg: Quantile Regression. R package version 4.98.*, [available at http://CRAN.R-project.org/package=quantreg].

Koenker, R., and G. Bassett (1978), Regression Quantiles, *Econometrica*, *46*(1), 33–50, doi:10.2307/1913643.

Kummerow, C., W. Barnes, T. Kozu, J. Shiue, and J. Simpson (1998), The tropical rainfall measuring mission(TRMM) sensor package, *J. Atmos. Ocean. Technol.*, *15*(3), 809–817, doi:10.1175/1520-0426(1998)015<0809:TTRMMT>2.0.CO;2.

Lau, K.-M., and H.-T. Wu (2011), Climatology and changes in tropical oceanic rainfall

characteristics inferred from Tropical Rainfall Measuring Mission (TRMM) data (1998–2009), *J. Geophys. Res.*, *116*(D17), D17111, doi:10.1029/2011JD015827.

Lenderink, G., and J. Attema (2015), A simple scaling approach to produce climate scenarios of local precipitation extremes for the Netherlands, *Environ. Res. Lett.*, *10*(8), 85001, doi:10.1088/1748-9326/10/8/085001.

Lenderink, G., and E. van Meijgaard (2008), Increase in hourly precipitation extremes beyond expectations from temperature changes, *Nat. Geosci.*, *1*(8), 511–514, doi:10.1038/ngeo262.

Lenderink, G., H. Y. Mok, T. C. Lee, and G. J. van Oldenborgh (2011), Scaling and trends of hourly precipitation extremes in two different climate zones – Hong Kong and the Netherlands, *Hydrol. Earth Syst. Sci.*, *15*(9), 3033–3041, doi:10.5194/hess-15-3033-2011.

Li, L., C. S. Ngongondo, C. Xu, and L. Gong (2013), Comparison of the global TRMM and WFD precipitation datasets in driving a large-scale hydrological model in southern Africa, *Hydrol. Res.*, *44*(5), 770, doi:10.2166/nh.2012.175.

Libertino, A., A. Sharma, V. Lakshmi, and P. Claps (2016), A global assessment of the timing of extreme rainfall from TRMM and GPM for improving hydrologic design, *Environ. Res. Lett.*, *11*(5), 54003, doi:10.1088/1748-9326/11/5/054003.

Lin, Y., M. Zhao, and M. Zhang (2015), Tropical cyclone rainfall area controlled by relative sea surface temperature., *Nat. Commun.*, *6*, 6591, doi:10.1038/ncomms7591.

Liu, C., and R. P. Allan (2012), Multisatellite observed responses of precipitation and its

extremes to interannual climate variability, *J. Geophys. Res. Atmos.*, *117*, D03101, doi:10.1029/2011JD016568.

Liu, S. C., C. Fu, C.-J. Shiu, J.-P. Chen, and F. Wu (2009), Temperature dependence of global precipitation extremes, *Geophys. Res. Lett.*, *36*(17), L17702, doi:10.1029/2009GL040218.

Maeda, E. E., N. Utsumi, and T. Oki (2012), Decreasing precipitation extremes at higher temperatures in tropical regions, *Nat. Hazards*, *64*(1), 935–941, doi:10.1007/s11069-012-0222-5.

Menne, M. J., I. Durre, R. S. Vose, B. E. Gleason, and T. G. Houston (2012), An Overview of the Global Historical Climatology Network-Daily Database, *J. Atmos. Ocean. Technol.*, *29*(7), 897–910, doi:10.1175/JTECH-D-11-00103.1.

Menne, M. J. et al. (2015), *Global Historical Climatology Network - Daily (GHCN-Daily)*, Version 3.22, NOAA National Climatic Data Center [available at http://doi.org/10.7289/V5D21VHZ].

Mishra, V., J. M. Wallace, and D. P. Lettenmaier (2012), Relationship between hourly extreme precipitation and local air temperature in the United States, *Geophys. Res. Lett.*, *39*(16), L16403, doi:10.1029/2012GL052790.

Molnar, P., S. Fatichi, L. Gaál, J. Szolgay, and P. Burlando (2015), Storm type effects on super Clausius–Clapeyron scaling of intense rainstorm properties with air temperature, *Hydrol. Earth Syst. Sci.*, *19*(4), 1753–1766, doi:10.5194/hess-19-1753-2015.

Nicholson, S. E. et al. (2003), Validation of TRMM and Other Rainfall Estimates with a High-Density Gauge Dataset for West Africa. Part II: Validation of TRMM Rainfall Products, *J. Appl. Meteorol.*, *42*(10), 1355–1368, doi:10.1175/1520-0450(2003)042<1355:VOTAOR>2.0.CO;2.

O'Gorman, P. A. (2012), Sensitivity of tropical precipitation extremes to climate change, *Nat. Geosci.*, *5*(10), 697–700, doi:10.1038/ngeo1568.

O'Gorman, P. A., and T. Schneider (2009), The physical basis for increases in precipitation extremes in simulations of 21st-century climate change., *Proc. Natl. Acad. Sci. U. S. A.*, *106*(35), 14773–7, doi:10.1073/pnas.0907610106.

Ochoa, A., L. Pineda, P. Crespo, and P. Willems (2014), Evaluation of TRMM 3B42 precipitation estimates and WRF retrospective precipitation simulation over the Pacific–Andean region of Ecuador and Peru, *Hydrol. Earth Syst. Sci.*, *18*(8), 3179–3193, doi:10.5194/hess-18-3179-2014.

Panthou, G., A. Mailhot, E. Laurence, and G. Talbot (2014), Relationship between Surface Temperature and Extreme Rainfalls: A Multi-Time-Scale and Event-Based Analysis, *J. Hydrometeorol.*, *15*(5), 1999–2011, doi:10.1175/JHM-D-14-0020.1.

Prasetia, R., A. R. As-syakur, and T. Osawa (2013), Validation of TRMM Precipitation Radar satellite data over Indonesian region, *Theor. Appl. Climatol.*, *112*(3–4), 575–587, doi:10.1007/s00704-012-0756-1.

Rasmussen, K. L., S. L. Choi, M. D. Zuluaga, and R. A. Houze (2013), TRMM precipitation bias in extreme storms in South America, *Geophys. Res. Lett.*, *40*(13), 3457–3461, doi:10.1002/grl.50651.

Rohde, R., R. a Muller, R. Jacobsen, E. Muller, D. Groom, and C. Wickham (2013a), A New Estimate of the Average Earth Surface Land Temperature Spanning 1753 to 2011, *Geoinformatic Geostatistics An Overv.*, *1*(1), 1–7, doi:http://dx.doi.org/10.4172/gigs.1000101.

Rohde, R., R. a Muller, R. Jacobsen, S. Perlmutter, A. Rosenfeld, J. Wurtele, J. Curry, C. Wickham, and S. Mosher (2013b), Berkeley Earth Temperature Averaging Process, *Geoinformatic Geostatistics An Overv.*, *1*(2), 1–13, doi:http://dx.doi.org/10.4172/gigs.1000103.

Romilly, T. G., and M. Gebremichael (2011), Evaluation of satellite rainfall estimates over Ethiopian river basins, *Hydrol. Earth Syst. Sci.*, *15*(5), 1505–1514, doi:10.5194/hess-15-1505-2011.

Roth, M., T. A. Buishand, and G. Jongbloed (2015), Trends in Moderate Rainfall Extremes: A Regional Monotone Regression Approach, *J. Clim.*, *28*(22), 8760–8769, doi:10.1175/JCLI-D-14-00685.1.

Seneviratne, S. et al. (2012), Changes in climate extremes and their impacts on the natural physical environment, in *Managing the Risk of Extreme Events and Disasters to Advance*

Climate Change Adaptation, edited by C. B. Field et al., pp. 109–230, Cambridge University Press, A Special Report of Working Groups I and II of the Intergovernmental Panel on Climate Change (IPCC). Cambridge, UK, and New York, NY, USA.

Shaw, S. B., A. A. Royem, and S. J. Riha (2011), The Relationship between Extreme Hourly Precipitation and Surface Temperature in Different Hydroclimatic Regions of the United States, *J. Hydrometeorol.*, *12*(2), 319–325, doi:10.1175/2011JHM1364.1.

Sheffield, J., G. Goteti, and E. F. Wood (2006), Development of a 50-Year High-Resolution Global Dataset of Meteorological Forcings for Land Surface Modeling, *J. Clim.*, *19*(13), 3088–3111, doi:10.1175/JCLI3790.1.

Su, F., Y. Hong, and D. P. Lettenmaier (2008), Evaluation of TRMM Multisatellite Precipitation Analysis (TMPA) and Its Utility in Hydrologic Prediction in the La Plata Basin, *J. Hydrometeorol.*, *9*(4), 622–640, doi:10.1175/2007JHM944.1.

Tan, X., and D. Shao (2016), Precipitation trends and teleconnections identified using quantile regressions over Xinjiang, China, *Int. J. Climatol.*, doi:10.1002/joc.4794.

Tian, Y., and C. D. Peters-Lidard (2010), A global map of uncertainties in satellite-based precipitation measurements, *Geophys. Res. Lett.*, *37*(24), L24407, doi:10.1029/2010GL046008.

Trenberth, K. E., and D. J. Shea (2005), Relationships between precipitation and surface temperature, *Geophys. Res. Lett.*, *32*(14), L14703, doi:10.1029/2005GL022760.

Trenberth, K. E., A. Dai, R. M. Rasmussen, and D. B. Parsons (2003), The changing character of precipitation, *Bull. Am. Meteorol. Soc.*, *84*(9), 1205–1217, doi:10.1175/BAMS-84-9-1205.

Utsumi, N., S. Seto, S. Kanae, E. E. Maeda, and T. Oki (2011), Does higher surface temperature intensify extreme precipitation?, *Geophys. Res. Lett.*, *38*(16), L16708, doi:10.1029/2011GL048426.

Ward, E., W. Buytaert, L. Peaver, and H. Wheater (2011), Evaluation of precipitation products over complex mountainous terrain: A water resources perspective, *Adv. Water Resour.*, *34*(10), 1222–1231, doi:10.1016/j.advwatres.2011.05.007.

Wasko, C., and A. Sharma (2014), Quantile regression for investigating scaling of extreme precipitation with temperature, *Water Resour. Res.*, *50*(4), 3608–3614, doi:10.1002/2013WR015194.

Wasko, C., and A. Sharma (2015), Steeper temporal distribution of rain intensity at higher temperatures within Australian storms, *Nat. Geosci.*, *8*(7), 527–529, doi:10.1038/ngeo2456.

Wasko, C., A. Sharma, and F. Johnson (2015), Does storm duration modulate the extreme precipitation-temperature scaling relationship?, *Geophys. Res. Lett.*, *42*(20), 8783–8790, doi:10.1002/2015GL066274.

Wasko, C., A. Sharma, and S. Westra (2016), Reduced spatial extent of extreme storms at higher temperatures, *Geophys. Res. Lett.*, *43*(8), 4026–4032, doi:10.1002/2016GL068509.

Wentz, F. J., L. Ricciardulli, K. Hilburn, and C. Mears (2007), How Much More Rain Will

Global Warming Bring?, *Science (80-.).*, *317*(5835), 233–235, doi:10.1126/science.1140746.

Westra, S., and S. A. Sisson (2011), Detection of non-stationarity in precipitation extremes using a max-stable process model, *J. Hydrol.*, *406*(1–2), 119–128, doi:10.1016/j.jhydrol.2011.06.014.

Westra, S., H. J. Fowler, J. P. Evans, L. . Alexander, P. Berg, F. Johnson, E. J. Kendon, G. Lenderink, and N. M. Roberts (2014), Future changes to the intensity and frequency of short-duration extreme rainfall, *Rev. Geophys.*, *52*(3), 522–555, doi:10.1002/2014RG000464.

Yue, Q., E. J. Fetzer, B. H. Kahn, S. Wong, G. Manipon, A. Guillaume, and B. Wilson (2013), Cloud-State-Dependent Sampling in AIRS Observations Based on CloudSat Cloud Classification, *J. Clim.*, *26*(21), 8357–8377, doi:10.1175/JCLI-D-13-00065.1.

Zipser, E. J., D. J. Cecil, C. Liu, S. W. Nesbitt, and D. P. Yorty (2006), Where are the most: Intense thunderstorms on Earth?, *Bull. Am. Meteorol. Soc.*, *87*(8), 1057–1071, doi:10.1175/BAMS-87-8-1057.

Zulkafli, Z., W. Buytaert, C. Onof, B. Manz, E. Tarnavsky, W. Lavado, and J.-L. Guyot (2014), A Comparative Performance Analysis of TRMM 3B42 (TMPA) Versions 6 and 7 for Hydrological Applications over Andean–Amazon River Basins, *J. Hydrometeorol.*, *15*(2), 581–592, doi:10.1175/JHM-D-13-094.1.

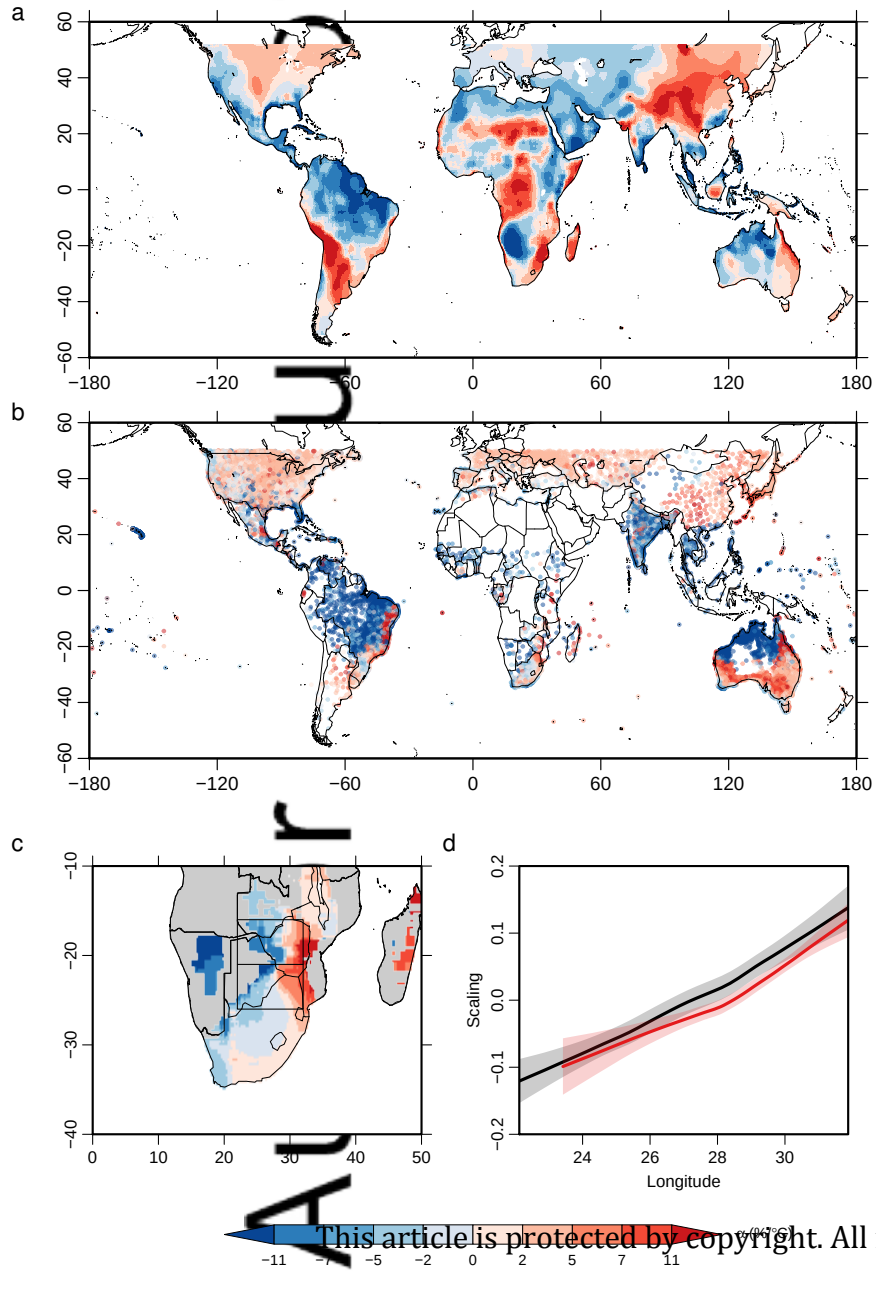

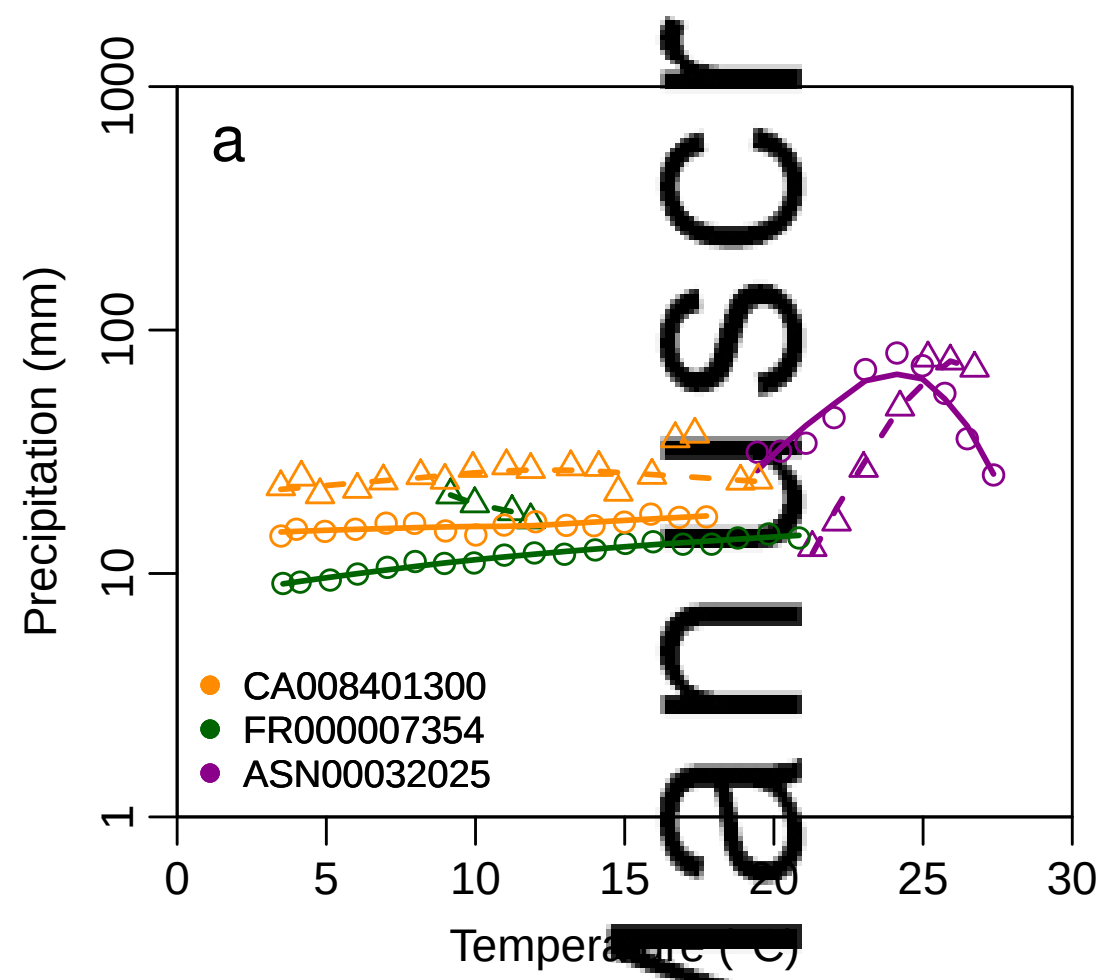
a
Precipitation (mm)
1000
100
10
1
0
5
10
15
20
25
30
CA008401300
FR000007354
ASN00032025

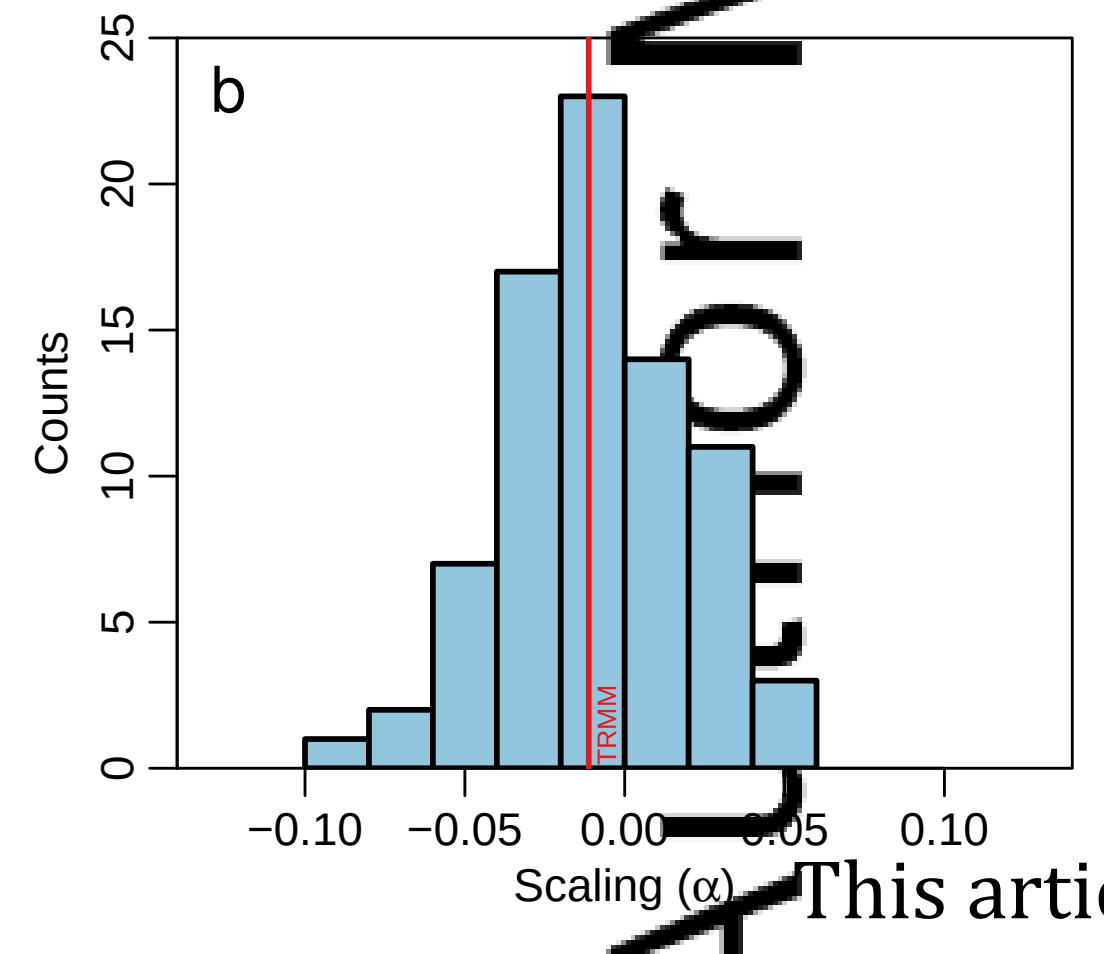
b
Counts
25
20
15
10
5
0
TRMM
−0.10
−0.05
0.00
0.05
0.10
Scaling (α)